EPJ Appl. Metamat. **13**, 15 (2026)

https://doi.org/10.1051/epjam/2026004

EPJ Applied Metamaterials

Available online at:
epjam.edp-open.org

ORIGINAL ARTICLE — OPEN ACCESS

Integrating vortex wave generation with broadband microwave attenuation using a multi-layer cascaded metasurface

Zhufang Hao[1], Yupeng Shi[2], and Yuping Duan[1,*]

[1] Key Laboratory of Solidification Control and Digital Preparation Technology (Liaoning Province), School of Materials Science and Engineering, Dalian University of Technology, Dalian 116085, China
[2] School of Material Science and Engineering, Henan University of Technology, Zhengzhou 450001, China

Received: 17 December 2025 / Accepted: 2 March 2026

Abstract. Developing electromagnetic metamaterials that simultaneously offer broadband response, a thin profile, and multifunctional capabilities remains a key challenge in stealth technology. Based on the Pancharatnam–Berry (PB) phase principle, this study proposes a multilayer cascaded geometric phase metasurface. By rotating the meta-atoms to introduce a controllable phase gradient, the metasurface efficiently converts incident circularly polarized waves into co-polarized reflected vortex waves, while leveraging electromagnetic coupling and resonance characteristics between the multilayer structures to achieve broadband energy dissipation. Experimental results demonstrate that this merely 2.72 mm thick multilayer cascaded structure achieves an effective absorption bandwidth of 7.9 GHz (8.1–16.0 GHz), representing a threefold increase over a single-layer design, and exhibits excellent radar cross-section (RCS) reduction performance. Near field and scattering confirm vortex wave generation with specific topological charges, revealing the intrinsic physical mechanism underlying broadband absorption and stealth through energy scattering across a wide angular domain. This study provides new insights for addressing the technical challenges of broadband and multifunctional absorption materials, laying an important foundation for the development of next-generation intelligent stealth metamaterials.

Keywords: Multilayer cascaded metasurface / microwave absorption / vortex wave / radar cross-section

1 Introduction

The rapid advancement of modern detection technologies has established electromagnetic stealth as a critical capability for advanced equipment and platforms [1–4]. However, conventional stealth approaches, which predominantly rely on a single physical mechanism such as energy absorption to reduce backscattering, struggle to meet the challenges of complex electromagnetic environments and broadband detection [5–12]. There is a pressing need to develop intelligent stealth technologies that integrate innovative mechanisms and multifunctional capabilities [13–16]. In this context, metamaterials, leveraging the powerful electromagnetic wave manipulation abilities of their subwavelength artificial structures, offer a novel pathway to achieve this goal. They have demonstrated revolutionary application prospects, including negative refraction [17], invisibility cloaking [18], and superlensing [19].

Existing metamaterials are typically composed of single or few-layer resonant elements, with their functionalities primarily achieved through phase distributions on a two-dimensional plane. Vortex waves carrying orbital angular momentum have garnered significant attention in the field of electromagnetic stealth due to their unique helical wavefronts and phase singularities [20–22]. Metamaterials, by designing the geometry and spatial arrangement of subwavelength meta-atoms, can introduce arbitrary phase discontinuities on their surfaces, thereby efficiently converting incident plane waves into vortex waves carrying specific topological charges. However, such "quasi-two-dimensional" metasurfaces often couple phase modulation with amplitude modulation, making it difficult to achieve pure phase modulation and resulting in low mode purity [23]. Furthermore, the resonant mechanisms underpinning the operation of these metamaterial units exhibit inherent strong dispersion [24–26], causing both phase compensation and polarization conversion efficiency to vary with frequency. This significantly limits their potential in broadband applications.

* e-mail: duanyp@dlut.edu.cn

To address the aforementioned limitations, researchers have drawn inspiration from multilayer thin-film systems in traditional optics and filtering theory in Fourier optics, proposing the innovative concept of multilayer cascaded metamaterials [27,28]. This architecture involves the three-dimensional stacking and spatial alignment of multiple metasurfaces, with distinct electromagnetic responses at subwavelength scales, with dielectric spacer layers separating the individual layers. The core advantage of the multilayer cascaded structure lies in its introduction of an entirely new design degree of freedom in the dimension along the wave propagation direction. By meticulously designing the structural parameters of each metasurface layer and the inter-layer spacing, the incident wave undergoes a complex, cascaded local interaction as it sequentially propagates through the stack. This interaction enables the entire structure to achieve synergistic manipulation and multidimensional synthesis of multiple wavefront degrees of freedom, including amplitude, phase, and polarization [29–30]. Its physical implications far exceed a simple superposition of single-layer functionalities, showcasing immense application potential in fields such as high-speed wireless communication [31], high-resolution imaging [32], compact optical systems [33], quantum information processing [34], and intelligent stealth technologies [35]. In particular, recent advances in microwave-frequency metamaterials have further demonstrated their capability in multifunctional wave manipulation and practical system-level integration, highlighting the growing importance of metasurface-based solutions in realistic electromagnetic environments [36].

In summary, to overcome the inherent limitations of conventional single-layer metasurfaces in simultaneously manipulating multiple electromagnetic degrees of freedom and integrating diverse functionalities, this paper proposes a multilayer cascaded three-dimensional architecture. The design first achieves synergistic control over multiple degrees of freedom of electromagnetic waves, including amplitude, phase, and polarization, by manipulating the spatial arrangement and inter-layer coupling of multiple metasurfaces. This enables the integration of vortex wave generation and broadband, efficient wave absorption functionalities on a compact platform. To realize precise manipulation of the electromagnetic wavefront, we constructed a multilayer cascaded metasurface based on the PB phase principle [37,38], composed of $FeCoNiSi_{0.3}Al_{0.3}$ high-entropy alloy (HEA) strips. By precisely controlling the rotation angle of the functional meta-atoms, a complete 2π phase coverage can be provided for incident circularly/linearly polarized waves, allowing for the flexible generation of customized multimode vortex waves. Furthermore, the study demonstrates that the strong electromagnetic coupling and resonance effects induced by cascading not only facilitate the construction of complex helical phase fronts but also enable efficient localization and dissipation of electromagnetic energy within the structure through multiple scattering and interference. This design integrates vortex wave manipulation and microwave attenuation, confirming the significant potential of the multilayer cascading strategy for expanding the dimensions of electromagnetic control and enhancing the overall performance of devices. It thereby opens a new pathway for developing advanced electromagnetic functional materials and devices.

2 Material selection and preparation

2.1 Material selection

In this study, iron (Fe), cobalt (Co), nickel (Ni), silicon (Si), and aluminum (Al) powders were used in the melting and rapid solidification process for the preparation of the $FeCoNiSi_{0.3}Al_{0.3}$ HEA. The $FeCoNiSi_{0.3}Al_{0.3}$ HEA is a type of electromagnetic wave absorbing material that combines both magnetic loss and dielectric loss mechanisms. The complex permittivity and permeability of this alloy system have been systematically characterized in our previous work [39], and the corresponding electromagnetic parameters were directly adopted in the metasurface design and numerical simulations of the present study.

The alloy ribbons prepared via melt-spinning can be employed to construct metasurfaces, achieving favorable impedance matching and excellent microwave attenuation performance [40]. In this alloy system, Fe contributes high saturation magnetization, while Co possesses a high Curie temperature. The Ni element, characterized by low magnetocrystalline anisotropy, is typically used to reduce the high magnetocrystalline anisotropy of Fe- and Co-based alloys, thereby improving the soft magnetic properties. Consequently, FeCoNi-based multi-principal element alloys often exhibit excellent soft magnetic properties and high Curie temperatures, which contribute to strong magnetic loss capabilities and good thermal stability. The addition of Si and Al helps reduce the magnetocrystalline anisotropy of the alloy system and enhances its plasticity, respectively. Based on the above considerations, the atomic ratio of the alloy components was determined as Fe:Co:Ni:Si:Al = 1:1:1:0.3:0.3.

2.2 Material preparation

(1) The preparation of $FeCoNiSi_{0.3}Al_{0.3}$ (HEA) ribbons was conducted in two sequential stages, as illustrated in Figure S1. The initial stage involved the preparation of a bulk alloy ingot, followed by the fabrication of HEA ribbons using a single-roller melt-spinning technique. In the first stage, a zirconium block was initially melted for approximately 20 s to establish an oxygen-free atmosphere within the arc furnace. Subsequently, the alloy sample was repeatedly flipped and remelted in a copper mold to form a bulk alloy ingot. After cooling for 15 min, the ingot was extracted and cut into appropriately sized pieces for the subsequent ribbon preparation process. During the second stage, the small alloy pieces were loaded into a quartz tube with a 1 mm diameter orifice at the bottom, while the copper roller rotated at a speed of 3000 rpm. When the alloy material within the quartz tube was heated to a molten state, the gas injection switch was activated. The molten alloy compressed against the surface of the copper roller undergoes rapid solidification and was ejected along the

roller to form ribbons. The resulting alloy ribbons exhibit a silver-white color, with a width of approximately 1 mm and a thickness of about 40 μm.

(2) The fabrication of the MLCGP metasurface proceeded as follows: The meta-atom had a length of $P = 18$ mm. The designed meta-atom pattern was printed onto a polycarbonate (PC) film, forming the geometric phase metasurface array. The fabricated $FeCoNiSi_{0.3}Al_{0.3}$ HEA meta-atoms, after being cut according to the substrate film pattern, were fixed onto the substrate using a thin layer of acrylate adhesive, resulting in the final single-layer geometric phase metasurface with a total thickness of 0.24 mm. Each metasurface layer, with dimensions of 200 × 200 mm, consisted of an 11 × 11 array of meta-atoms arranged according to the PB phase gradient. The MLCGP metasurface, composed of three stacked vortex metasurface layers, featured twist angles of 0°, 15°, and 30° from top to bottom, respectively. PC spacers with a relative permittivity (ε_r) of 2.95 were used between layers, with an interlayer separation (d) of 1 mm for both intervals, resulting in a total thickness of 2.72 mm. The detailed structure is illustrated in Figure 2h. As PC is a highly transparent material, the functionality of a single-layer geometric phase metasurface relies solely on the two-dimensional design of the surface meta-atoms, resulting in relatively limited wavefront control capability. In contrast, the MLCGP metasurface constitutes a three-dimensional control system. It enables electromagnetic waves to undergo multiple scattering and interference events between the vertically stacked layers, thereby providing more flexible wavefront shaping capabilities. Furthermore, the overlapping and coupling of electromagnetic fields among the three independent resonators facilitate the formation of a flat, broad absorption band, achieving efficient electromagnetic energy dissipation.

3 Design strategy

The PB phase operates by rotating subwavelength unit structures. This rotation enables the conversion of the polarization state of incident electromagnetic waves while simultaneously introducing a phase shift, proportional to the rotation angle of the unit, in either the co-polarized or cross-polarized channel. This mechanism facilitates wavefront manipulation and polarization control, allowing for the generation of vortex waves with specific properties.

Vortex waves carry different orthogonal components characterized by their topological charge (l). With rational design of the meta-atom dimensions and structural morphology, rotating the meta-atom through an arbitrary angle between 0 and π can induce a corresponding phase shift covering the full range of 0 to 2π. This makes it possible to design metasurfaces that generate vortex waves carrying different topological charges. The topological charge (l) of a vortex wave is expressed by the equation [41]:

$$l = \frac{1}{2\pi} \times \oint_C \nabla \emptyset(\mathbf{r}) dr \tag{1}$$

where l is the topological charge, $\emptyset$ is the phase distribution, C is a closed path encircling a phase singularity, and dr is the infinitesimal displacement vector along the integration path. The value of l reflects the degree of phase change around a singular region in space. The phase singularity is the point where different phases converge, and the phase is undefined (or zero), implying the absence of electromagnetic energy at the singularity point [42].

The Jones matrix is an effective tool for analyzing the incident and scattered fields of anisotropic units in a metasurface, linking the reflected field to the incident field via reflection coefficients. For a reflective meta-atom rotated by an angle θ, the reflection matrix is expressed as [43,44]

$$R_{xy}^{\theta} = \begin{bmatrix} \cos\theta & -\sin\theta \\ \sin\theta & \cos\theta \end{bmatrix}^{-1} \begin{bmatrix} r_{xx} & r_{xy} \\ r_{yx} & r_{yy} \end{bmatrix} \begin{bmatrix} \cos\theta & -\sin\theta \\ \sin\theta & \cos\theta \end{bmatrix}. \tag{2}$$

The reflection matrix under circularly polarized wave excitation can be represented as

$$R_{lr}^{\theta} = \begin{bmatrix} 1 & -j \\ 1 & \mathrm{j} \end{bmatrix}^{-1} R_{xy}^{\theta} \begin{bmatrix} 1 & -j \\ 1 & \mathrm{j} \end{bmatrix}. \tag{3}$$

Substituting equation (2) into equation (3) yields the reflection matrix for circularly polarized incidence:

$$r_{ll} = 0.5[(r_{xx} - r_{yy}) + j(r_{xy} + r_{yx})]e^{-2jk\theta} \tag{4a}$$

$$r_{lr} = 0.5[(r_{xx} + r_{yy}) + j(r_{yx} - r_{yx})] \tag{4b}$$

$$r_{rl} = 0.5[(r_{xx} + r_{yy}) - j(r_{yx} - r_{xy})] \tag{4c}$$

$$r_{rr} = 0.5[(r_{xx} - r_{yy}) - j(r_{xy} + r_{yx})]e^{2jk\theta}. \tag{4d}$$

Here, r_{xx}, r_{yy}, r_{ll}, and r_{rr} are the co-polarized reflection coefficients under normal incidence for x-, y-, left-hand circularly polarized (LHCP), and right-hand circularly polarized (RHCP) waves, respectively. Similarly, r_{xy}, r_{yx}, r_{lr}, and r_{rl} are the corresponding cross-polarized reflection coefficients. According to equations (4a) and (4d), a discrete phase change of $e^{-2j\theta}(e^{2j\theta})$ can be introduced by a meta-atom with a rotation angle θ.

For a reflective meta-atom, if it possesses mirror symmetry with respect to the xoz or yoz plane, its Jones matrix should satisfy $r_{xy} = r_{yx} = 0$. This implies that a meta-atom with this symmetric structure has no cross-polarization conversion terms. To achieve high angular momentum conversion efficiency over a broad frequency range, the meta-atom should satisfy the following conditions:

$$|r_{xx}| = |r_{yy}| \approx 1 \tag{5a}$$

$$\angle r_{xx} - \angle r_{yy} \approx \pi \tag{5b}$$

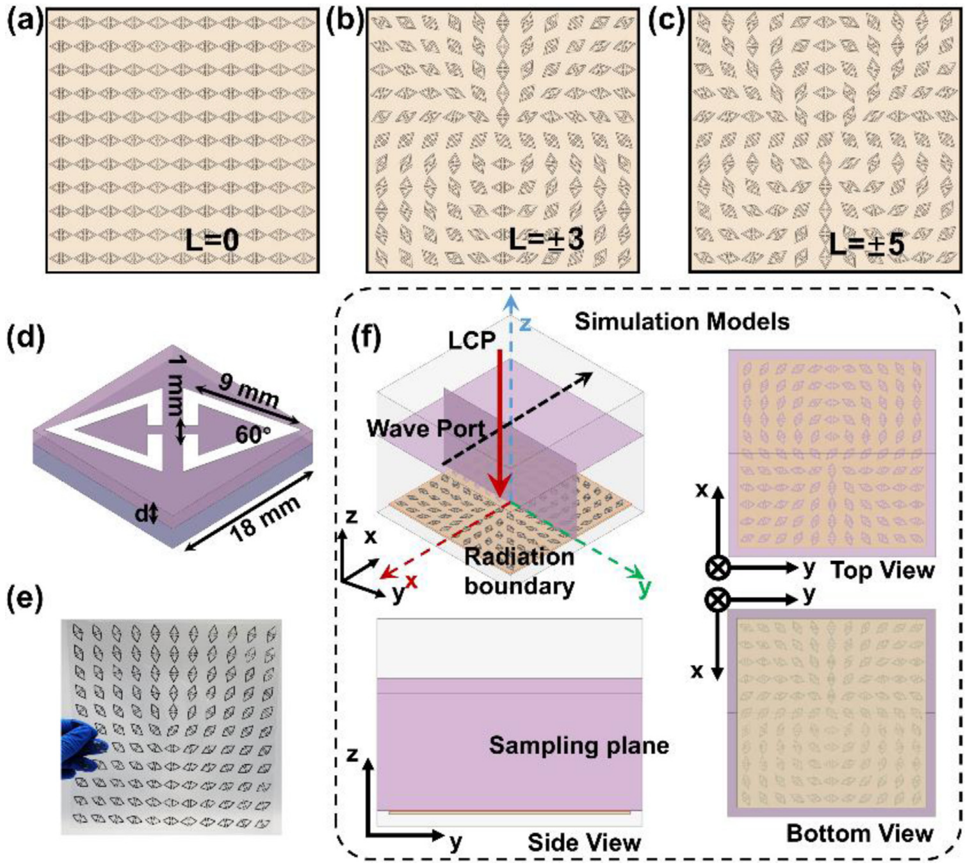

Fig. 1. The layout of the proposed metasurfaces for (a) $l = 0$, (b) $l = \pm 3$, and (c) $l = \pm 5$ OAM modes. (d) Schematic diagram of the structural unit. (e) Optical photograph of the fabricated geometric phase metasurface. (f) Schematic of the 3D HFSS simulation model.

As shown in Figure 1d, this study is based on the spin angular momentum (SAM) to orbital angular momentum (OAM) conversion concept. Symmetric split triangular meta-atoms with a specific rotation angle θ are arranged on a flexible substrate. The geometric parameters are side length $b = 9$ mm, metal thickness $h_1 = 0.04$ mm, gap width $w = 1$ mm, and vertex angle $\alpha = 60°$. The insulating dielectric is PC (meta-atom period $p = 18$ mm, relative permittivity $\varepsilon_r = 2.95$).

After determining the relationship between the two-dimensional vortex phase distribution and the phase parameters, a geometric mapping program was written in MATLAB to automatically generate the layout of the geometric phase metasurface carrying different modes. The numerical results were then imported into CAD (computer-aided design) software for printing the metasurface substrate film. Finally, co-simulation using MATLAB and HFSS (high-frequency structure simulator) was employed to obtain the near-field and far-field characteristics of the vortex wave. A schematic of the simulation model and setup is shown in Figure 1f. The reflective metasurface consists of an 11×11 array of rotating meta-atoms. The corresponding topological charges are shown in Figure 1 as (a) $l = 0$, (b) $l = \pm 3$, and (c) $l = \pm 5$. The sign of the topological charge depends on the spin state of the incident wave. Figure 1e shows a photograph of the fabricated geometric phase metasurface.

4 Results and discussion

4.1 Absorbing performance of the MLCGP metasurface

The reflectivity of geometric phase metasurfaces with different numbers of layers under incident wave illumination was evaluated in a microwave anechoic chamber to investigate the impact of multilayer cascading on microwave attenuation performance. Prior to this, we examined the reflection loss performance of metasurfaces without introducing a discrete phase shift (i.e., with meta-atom rotation angle $\theta = 0$, indicating only periodic arrangement without a phase gradient) for different dielectric substrate thicknesses ($d = 1$, 2, and 3 mm). As shown in Figure 2a, the reflection loss performance under this condition is poor, struggling to achieve an effective absorption of -10 dB. Geometric phases corresponding to two different vortex modes ($l = -3$ and -5) were then introduced into single-layer metasurfaces with dielectric thicknesses of 2 and 3 mm. As shown in Figures 2b and 2c, the microwave absorption efficiency shows insignificant improvement for the 2 mm thickness case. In contrast, the microwave attenuation performance is significantly enhanced for the 3 mm thick geometric phase metasurface. Furthermore, the attenuation performance improves as the mode number ($|l|$) increases.

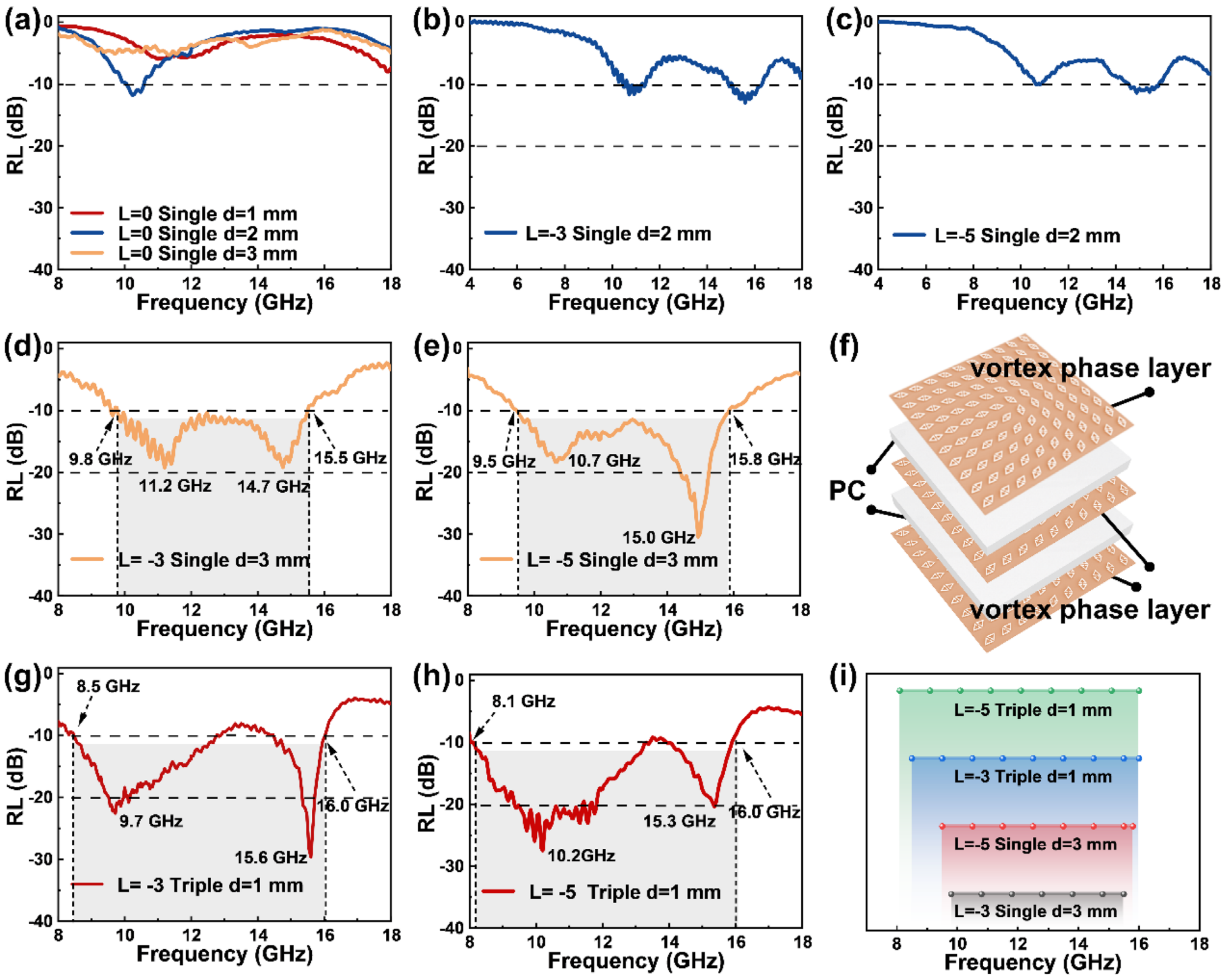

Fig. 2. Electromagnetic performance of single-layer and MLCGP metasurfaces. (a) Reflection loss of single-layer metasurfaces with different thicknesses at $l = 0$. Reflection loss of a 2 mm-thick single-layer metasurface at (b) $l = -3$ and (c) $l = -5$. Reflection loss of a 3 mm-thick single-layer metasurface at (d) $l = -3$ and (e) $l = -5$. (f) Schematic diagram of the MLCGP metasurface structure. Reflection loss of the MLCGP metasurface at (g) $l = -3$ and (h) $l = -5$. (i) Effective absorption bandwidth before and after cascading.

The thickness of an absorbing material is a critical parameter for assessing its application potential. Therefore, as illustrated in Figure 2f, this work cascades three geometric phase metasurfaces with different rotation angles, with the interlayer dielectric spacing reduced to 1 mm. As shown in Figures 2g and 2h, benefiting from the multilayer cascaded architecture, the structure maintains stable and efficient microwave attenuation performance even when its total thickness is reduced by approximately 30% compared to a 3 mm-thick single-layer dielectric metasurface.

It should be noted that within the 13–14 GHz frequency range, the MLCGP metasurface does not fully satisfy the −10 dB absorption criterion, and its attenuation performance in this narrow band appears slightly inferior to that of the 3 mm single-layer structure. This localized reduction can be attributed to the redistribution of resonant modes and the modified impedance matching condition induced by strong interlayer electromagnetic coupling. The introduction of multiple reflective interfaces alters the phase accumulation and interference pathways inside the structure, and constructive interference may occur at specific frequencies, partially weakening the destructive interference mechanism responsible for efficient absorption. Nevertheless, this trade-off is confined to a limited spectral region and does not compromise the overall broadband enhancement achieved through cascading.

Compared to the single-layer structure, the MLCGP architecture exhibits a significantly expanded effective absorption bandwidth, reaching 7.9 GHz (RL ≤ -10 dB, covering 8.1–16.0 GHz) under the $l = -5$ vortex mode. Figure 2i visualizes the comparison of effective absorption bandwidth before and after cascading. The performance advantage of the MLCGP structure is even more pronounced for the −20 dB reflection loss metric, which characterizes deep absorption. Its applicable bandwidth at this level is approximately three times wider than that of the single-layer structure. This enhancement is attributed to the strong electromagnetic field localization and interlayer interference effects induced by the MLCGP structure. The three layers of meta-atoms, combined with the PC dielectric spacers, form a sophisticated multiple-reflection system. When electromagnetic waves are incident, the reflected waves generated from each layer interfere with each other, and through precise phase design, destructive interference is achieved within specific frequency bands. This phenomenon effectively "traps" the electromagnetic energy within the structure, where it is subsequently dissipated efficiently through ohmic loss and diffraction loss in the metallic microstructures. This implies that for high-performance applications such as radar stealth and electromagnetic compatibility, multilayer cascaded metamaterials show great potential for achieving extremely low electromagnetic wave backscattering over a broad frequency band, significantly enhancing stealth or shielding effectiveness.

4.2 RCS reduction of the MLCGP metasurface

A lower reflection loss indicates that a larger portion of the incident electromagnetic energy is absorbed and converted within the structure, thereby reducing the energy scattered back into free space. This directly affects the magnitude and angular distribution of the RCS. To evaluate the scattering behavior, bistatic simulations were performed by varying the receiving angle while fixing the azimuth angle at $\varphi = 0°$. Figures 3a and 3c present the corresponding one-dimensional RCS angular distributions with θ ranging from $-180°$ to $180°$ for $l = -3$ (9.7 GHz) and $l = -5$ (10.2 GHz), respectively.

These RCS fluctuations originate from the coherent interference of waves scattered by the discrete meta-atoms. Maxima in the RCS correspond to directions where constructive interference dominates, forming strong scattering directions, whereas minima arise from destructive interference and represent stealth-favorable directions. When the topological charge increases from $l = -3$ to $l = -5$, the angular fluctuation density becomes more pronounced. This behavior reflects the more rapid azimuthal phase variation associated with higher-order vortex modes, which enhances the complexity of spatial phase coupling and leads to a denser interference pattern.

Figures 3b and 3d show three-dimensional far-field scattering patterns at representative operating frequencies. Figures 3a and 3c correspond to two-dimensional angular RCS curves extracted from the $\varphi = 0$ plane of the respective 3D scattering patterns in Figures 3b and 3d. This relationship clarifies the direct correspondence between the 2D cross-sectional results and the full spatial scattering distributions.

Compared with the lower-order mode, the higher-order vortex excitation results in a more evident deviation of energy from the conventional specular reflection direction, accompanied by a broadened and partially split main scattering lobe. At higher frequencies, as shown in Figure S2, the scattered energy is mainly concentrated along the propagation axis and within a relatively narrow angular ring, with additional energy appearing along diagonal directions. This indicates a stronger axial confinement of the scattered field at elevated frequencies.

Under linearly polarized illumination, the incident field can be decomposed into two circularly polarized components with opposite handedness. Due to the geometric-phase mechanism, these two components acquire opposite phase gradients, leading to the simultaneous excitation of conjugate vortex modes with topological charges of $+l$ and $-l$. The far-field superposition of these modes suppresses the ideal phase singularity at the beam center, resulting in residual on-axis scattering and a partially filled vortex core. Nevertheless, the geometric phase still effectively redistributes the scattered energy away from the mirror-reflection direction, producing the observed lobe broadening and "aperture" effect. This demonstrates that even under linear polarization excitation, the MLCGP metasurface retains its capability to manipulate electromagnetic wavefronts and steer energy flow, offering potential advantages for applications such as channel multiplexing and adaptive beam control in radar and wireless communication systems.

4.3 Analysis of the absorption mechanism in a MLCGP metasurface

Achieving high-quality OAM beams in the microwave regime presents significant technical challenges. Unlike at optical frequencies, generating ideal planar wavefronts is difficult in the microwave band. This leads to prevalent issues such as wavefront distortion and excessive divergence angles in vortex waves generated by geometric-phase-based metasurfaces, severely limiting their applicability in long-distance communication. However, these seemingly detrimental characteristics demonstrate unique value in the realm of electromagnetic stealth. The pronounced beam divergence and phase distortion facilitate the rapid dissipation of electromagnetic energy and effectively reduce the target's RCS. Based on this premise, to further validate the broadband microwave attenuation characteristics of the MLCGP metasurface, full-wave simulations were conducted to analyze the near-field and far-field vortex wave properties under LHCP wave excitation. The monitoring plane, set parallel to the metasurface (xoy plane) with dimensions of 200×200 mm, was positioned 100 mm above the structure. Near-field observations and mode spectrum analyses were performed for the generated $l = -3$ and $l = -5$ vortex waves under LHCP plane wave excitation with an electric field oriented along the x-direction at different frequencies. The electromagnetic simulation results, shown in Figure S3, indicate well-dispersed electric field energy across various frequencies. When the incident wave frequency was 9.7 GHz, as shown in Figure 4a, ring-like electric field amplitude patterns were observed in the LHCP field at different phases. The electric field amplitude was significantly reduced along the propagation axis (i.e., the phase singularity), while the energy was concentrated within a distinct concentric annular region. Simultaneously, the spatial distribution of the electric field phase exhibited a dynamic pattern, rotating regularly over time around the beam center. This rotation does not represent a net flow of energy but is a direct manifestation of the wavefront's helical phase structure evolving in the time domain, with a

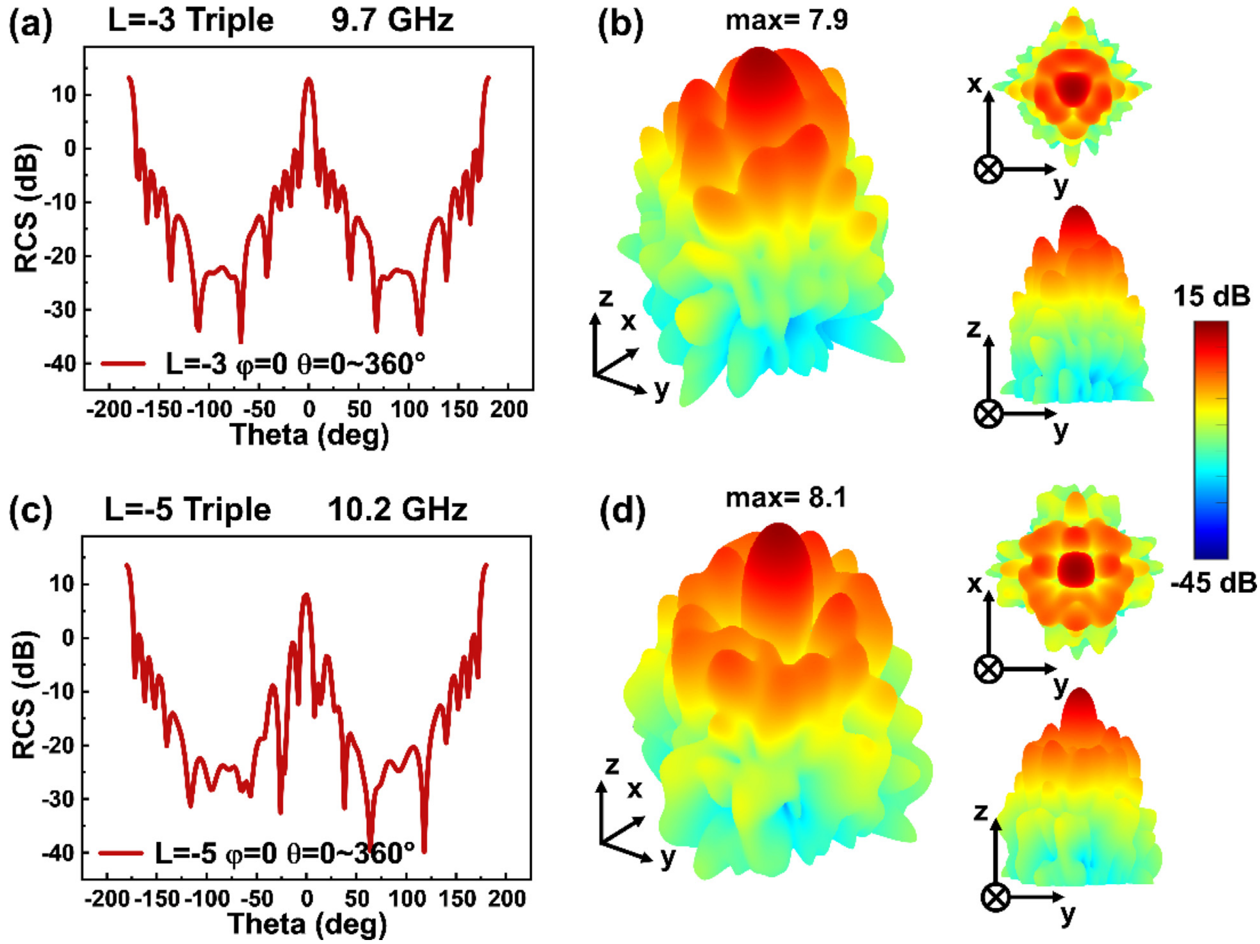

Fig. 3. Bistatic RCS characteristics of the vortex metasurfaces. (a, c) Bistatic RCS patterns at an azimuth angle of $\varphi = 0°$. (b, d) Three-dimensional bistatic RCS distributions at 7.9 GHz for the $l = -3$ MLCGP metasurface and at 8.1 GHz for the $l = -5$ MLCGP metasurface.

complete rotation period corresponding to the oscillation period of the electromagnetic wave. This dynamic phenomenon confirms that the metasurface successfully converted linear momentum into orbital angular momentum, generating vortex waves in the corresponding modes.

Furthermore, this cascading configuration establishes a multi-resonant interference system. Part of the incident wave is successively reflected and re-injected between adjacent layers, forming repeated phase accumulation and multiple scattering pathways. The constructive and destructive interference among these coupled resonant modes dynamically redistributes the electromagnetic energy inside the structure. As a result, localized electric and magnetic field enhancement occurs within specific regions of the high-entropy alloy strips and dielectric layers, effectively increasing ohmic loss and dielectric dissipation.

More importantly, the geometric-phase-induced spatial phase gradient modifies the wavefront of the reflected fields at each interface, suppressing coherent specular reflection and promoting angular dispersion. The combined effects of interlayer coupling, resonance hybridization, and phase-gradient-induced wavefront distortion therefore enhance both internal energy trapping and external scattering diffusion. This synergistic mechanism explains the observed broadband reflection loss reduction and RCS suppression.

Further analysis was conducted on the three-dimensional scattered fields under LHCP wave incidence at different frequencies. The results, as shown in Figure S4, reveal that for a beam with the same topological charge, its radiation aperture angle systematically decreases with increasing frequency. The underlying reason is that the fixed phase profile introduced by the geometric phase equivalently produces a stronger local phase gradient at shorter wavelengths. This enhanced phase gradient effectively focuses the wavefront, partially compensating for the divergence effect caused by a high topological charge, thereby leading to a reduced radiation aperture at higher frequencies. As shown in Figure 4b, under a constant operating frequency, the main lobe radiation aperture angle of the $l = -5$ vortex wave in three-dimensional space is noticeably larger than that of the $l = -3$ configuration, and the main lobe radiation intensity is also significantly lower. This effectively demonstrates the propagation characteristics of vortex waves: namely, a larger magnitude of l leads to more pronounced divergence of the vortex wavefront, which is consistent with the theoretical design.

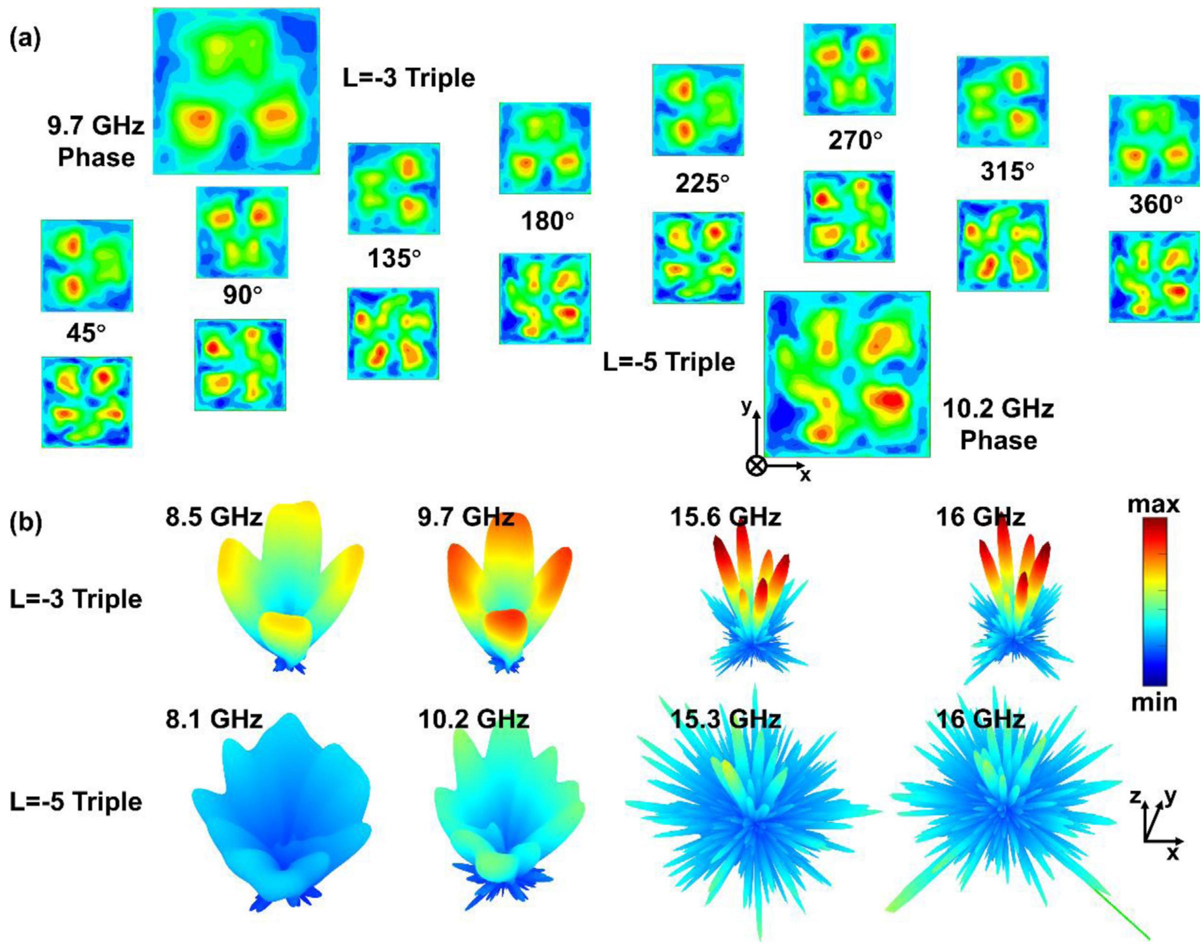

Fig. 4. Near-field and far-field characteristics of the MLCGP metasurface. (a) Electric field amplitude distributions in the near-field region under different phase conditions for the MLCGP metasurfaces with $l = -3$ and $l = -5$. (b) Three-dimensional far-field radiation patterns for the MLCGP metasurfaces with $l = -3$ and $l = -5$.

As the mode number of the MLCGP metasurface increases, the electromagnetic energy at the central phase singularity correspondingly weakens. The null region at the vortex wave center progressively expands with increasing propagation distance, primarily determined by the unique phase front morphology of the vortex wave. The far-field diffusion characteristics of vortex waves prevent them from propagating over long distances. However, this very energy attenuation and dissipation are highly desirable in microwave stealth applications. If a stealth material can effectively convert incident electromagnetic waves into vortex waves, it could potentially enable perfect stealth behavior through the synergistic effects of mechanisms like polarization conversion loss and far-field diffusion attenuation.

Based on the foregoing analysis, we have elucidated the intrinsic relationship among the radiation aperture angle, frequency, and topological charge and have experimentally validated the characteristic divergence and attenuation behaviors of vortex waves during propagation. Building upon this foundation, and to further assess the feasibility and comprehensive performance of this stealth approach, a systematic comparison was conducted between the designed MLCGP metasurface and several typical absorbing materials. As summarized in Table 1, the MLCGP metasurface holds significant advantages in terms of effective microwave absorption bandwidth and overall thickness. Specifically, while ensuring highly efficient microwave absorption, the total thickness of this metasurface is effectively controlled, which is crucial for meeting the requirements of lightweight and thin designs in practical applications. Furthermore, the metasurface fabricated using $FeCoNiSi_{0.3}Al_{0.3}$ HEA ribbons exhibits an areal density of only 0.75 kg/m^2. This low areal density characteristic not only reduces the overall weight of the material but also opens up possibilities for its application in fields such as aerospace, thereby further enhancing the comprehensive performance and application potential of this metasurface.

5 Conclusion and outlook

The MLCGP metasurface achieves broadband microwave absorption performance at a thinner thickness by synergistically utilizing the polarization conversion characteristics and wavefront manipulation capabilities of electromagnetic waves. Based on the PB phase principle, this structure converts incident plane waves into co-polarized reflected vortex waves, enabling highly

Table 1. Properties comparison between this prepared metamaterial and others.

Material	Structure	Thickness (mm)	Effective absorption bandwidth (GHz) (RL≤ −10 dB)	References
FCIP	Porous coating	6	18	[45]
$Fe_{60}Co_{20}Ni_{10}Si_{6.5}Al_{3.5}$	Ribbons	20	5.04	[40]
$FeCoNiSi_xAl_{0.4}$	Powder	2	4.28	[46]
polymeric GN	Multilayer	3.5	1.9	[47]
Cu	Hybrid metasurface	4.1	2	[48]
CIP/PU	Three biomimetic structures	3	6.94	[49]
Al/CIP	Fractal structure	2.24	1.38	[50]
NHCS@Fe/Fe_3O_4-700	multilayered open-ring configuration	2.37	6.59	[51]
Cu, FR-4	Fractal structure	3.2	3.36	[52]
ITO dielectric	Sandwiched structure	3.5	2.5	[53]
RGO	Pyramid structure	9	10	[54]
HEA ribbons	Vortex metasurfaces	2.72	7.9	This work

efficient energy dissipation. Experimental results demonstrate that the MLCGP metasurface, with a thickness of only 2.72 mm, attains an effective absorption bandwidth of 7.9 GHz (8.1–16.0 GHz). This represents a 35% increase compared to a single-layer geometric-phase metasurface with a thickness of 3.24 mm, along with excellent RCS reduction. Through OAM phase analysis and three-dimensional scattered field characterization, the successful generation of vortex waves with specific topological charges has been confirmed. Furthermore, the core mechanism of achieving broadband absorption and scattering reduction by dispersing energy across wide angular spaces has been revealed from a physical perspective. This work establishes a new paradigm for the development of novel, thin-layer absorbing materials based on wavefront shaping.

Funding

The Program for the National Natural Science Foundation of China (No. 52071053) and the Fundamental Research Funds for the Central Universities (No. DUT24GF102).

Conflicts of Interest

There are no conflicts to declare.

Data availability statement

All data supporting the findings of this study are included within the manuscript and its supplementary materials. Additional raw datasets generated during the study are available from the corresponding author upon reasonable request.

Author contribution statement

Zhufang Hao designed the study, drafted the manuscript, and conducted primary data analysis; Yupeng Shi performed the simulations and fabricated the metasurface samples; Yuping Duan supervised the project, revised and polished the manuscript, and ensured overall scientific accuracy. All authors contributed to discussion and approved the final manuscript.

Supplementary material

Fig S1 Preparation of HEA ribbons.
Fig S2 Three-dimensional bistatic RCS distributions at 15.6 GHz for the $l = -3$ MLCGP metasurface and at 15.3 GHz for the $l = -5$ MLCGP metasurface.
Fig S3 Near-field characteristics of the multilayer vortex metasurface. Electric field amplitude distributions in the near-field region for the multilayer vortex metasurfaces with $l = -3$ and $l = -5$.
Fig S4 Three-dimensional far-field radiation patterns for the multilayer vortex metasurfaces with $l = -3$ and $l = -5$.

The Supplementary material is available at https://www.epjam.edp-open.org/10.1051/epjam/2026004/olm.

References

1. G. Wang, D. Li, W. Liao, et al., Multifunctional metamaterial with reconfigurable electromagnetic scattering properties for advanced stealth and adaptive applications, Adv. Mater. **36**, 2408216 (2024)
2. Y. Wu, S. Tan, Y. Zhao, et al., Broadband multispectral compatible absorbers for radar, infrared and visible stealth application, Prog. Mater. Sci. **135**, 101088 (2023)
3. Y.Y. Xie, S.C. Chen, G. Wu, et al., Leaf-inspired hierarchical carbon with "disordered skin-ordered core" architecture for compatible radar-infrared stealth, Adv. Funct. Mater. **36**, e17656 (2025)
4. W. Kang, Y. Shen, T. Yang, et al., Multifunctional submicron SiC fibers for extreme environments: superior electromagnetic absorption and high-temperature performance, Adv. Funct. Mater. **35**, 2415432 (2025)

5. S. Ji, M. Qin, J. Zhao, et al., Biomimetic water-based metamaterial absorber for ultrabroadband radar stealth, Adv. Mater. **38**, e07439 (2025)
6. B. Dai, Y. Ma, F. Dong, et al., Overview of MXene and conducting polymer matrix composites for electromagnetic wave absorption, Adv. Compos. Hybrid Mater. **5**, 704 (2022)
7. S. Liu, Y. Zhou, F. Zhang, et al., A novel full-band microwave absorber based on scattering enhanced prism-honeycomb nested structure, Adv. Funct. Mater. **35**, 2422666 (2025)
8. W. Kang, Y. Shen, T. Yang, et al., Multifunctional submicron SiC fibers for extreme environments: superior electromagnetic absorption and high-temperature performance, Adv. Funct. Mater. **35**, 2415432 (2025)
9. Z. Jiang, Y. Gao, Z. Pan, et al., Pomegranate-like ATO/SiO2 microspheres for efficient microwave absorption in wide temperature spectrum, J. Mater. Sci. Technol. **174**, 195 (2024)
10. W. Deng, D. Zhi, J. Li, et al., Electromagnetic oscillation induced graphene-based aerogel microspheres with dual-chamber achieving high-performance broadband microwave absorption, Compos. Part B Eng. **271**, 111149 (2024)
11. Z. Qu, J. Hao, H. Jing, et al., An ultra-thin ultra-broadband microwave absorber for radar stealth, Adv. Compos. Hybrid Mater. **5**, 1778 (2022)
12. X. Su, J. Wang, T. Liu, et al., Controllable atomic migration in microstructures and defects for electromagnetic wave absorption enhancement, Adv. Funct. Mater. **34**, 2403397 (2024)
13. C. Li, L. Liang, B. Zhang, et al., Magneto-dielectric synergy and multiscale hierarchical structure design enable flexible multipurpose microwave absorption and infrared stealth compatibility, Nano-Micro Lett. **17**, 40 (2025)
14. G. Wang, D. Li, W. Liao, et al., Agile stealth: bioinspired metamaterials with continuous dynamic tuning, Adv. Mater. e11070 (2025).
15. J. Qin, Y. Shi, S. Jiang, et al., Ultrabroadband and >93% microwave absorption enabled by "doped" water meta-atom lattice with subwavelength thickness, Adv. Mater. **36**, 2411153 (2024)
16. C. Qian, B. Zheng, Y. Shen, et al., Deep-learning-enabled self-adaptive microwave cloak without human intervention, Nat. Photonics **14**, 383 (2020)
17. Y. Liu, G.P. Wang, J.B. Pendry, et al., All-angle reflectionless negative refraction with ideal photonic Weyl metamaterials, Light Sci. Appl. **11**, 276 (2022)
18. T. Cai, B. Zheng, J. Lou, et al., Experimental realization of a superdispersion-enabled ultrabroadband terahertz cloak, Adv. Mater. **34**, 2205053 (2022)
19. Y. Gelkop, F. Di Mei, S. Frishman, et al., Hyperbolic optics and superlensing in room-temperature KTN from self-induced K-space topological transitions, Nat. Commun. **12**, 7241 (2021)
20. X.G. Zhang, W.X. Jiang, H.L. Jiang, et al., An optically driven digital metasurface for programming electromagnetic functions, Nat. Electron. **3**, 165 (2020)
21. L. Zhang, R.Y. Wu, G.D. Bai, et al., Transmission-reflection-integrated multifunctional coding metasurface for full-space controls of electromagnetic waves, Adv. Funct. Mater. **28**, 1802205 (2018)
22. M. Liu, Z. Wu, L. Yang, et al., Finite-sized atom reconstruction enhanced high-frequency multi-domain magnetic response, Adv. Funct. Mater. **33**, 2307943 (2023)
23. F. Mei, G. Qu, X. Sha, et al., Cascaded metasurfaces for high-purity vortex generation, Nat. Commun. **14**, 6410 (2023)
24. Z. Qu, H. Jing, H. Deng, et al., Ultra-wideband electromagnetic interference suppression lightweight metamaterial absorber based on S/C/X frequency band, Adv. Compos. Hybrid Mater. **6**, 156 (2023)
25. Z. Ren, Z. Yang, W. Mu, et al., Ultra-broadband perfect absorbers based on biomimetic metamaterials with dual coupling gradient resonators, Adv. Mater. **37**, 2416314 (2025)
26. Q. Huang, W. Xie, F.Z. Alqahtany, et al., Study on thin-layer broadband metamaterial absorber based on composite multi-opening ring pattern of magnetic dielectric layers, Adv. Compos. Hybrid Mater. **8**, 180 (2025)
27. C.Y. Shen, P. Batoni, X. Yang, et al., Broadband unidirectional visible imaging using wafer-scale nano-fabrication of multilayer diffractive optical processors, Light Sci. Appl. **14**, 267 (2025)
28. J. Azana, Orbital angular momentum, intertwining with Fourier optics, Nat. Photonics **19**, 340 (2025)
29. X. Xie, Y. Huang, Z. Yang, et al., Diatom cribellum-inspired hierarchical metamaterials: unifying perfect absorption toward subwavelength color printing, Adv. Mater. **36**, 2403304 (2024)
30. X.M. Liang, Q.F. Xuan, H.H. Li, et al., Multifunctional hierarchical BN/MXene-Fe3O4 aerogel for efficient thermal management and ultra-broadband microwave absorption, Chem. Eng. J. **523**, 168409 (2025)
31. Y. Ra'di, N. Nefedkin, P. Popovski, et al., Metasurfaces for next-generation wireless communication systems, Natl. Sci. Rev. **10**, nwad140 (2023)
32. L.S. Zeng, Z.B. Lin, Z.L. Li, et al., High-resolution manifold acoustic holography based on high-pixel-array binary metasurfaces, Adv. Mater. **37**, 2420229 (2025)
33. T. Phan, D. Sell, E.W. Wang, et al., High-efficiency, large-area, topology-optimized metasurfaces, Light Sci. Appl. **8**, 48 (2019)
34. G. Wu, F. Yan, L. Liang, et al., Exciton-photon coupling microcavity as a selective biosensing platform for nonlocal terahertz metamaterials, Adv. Sci. **12**, 2416951 (2025)
35. W. Ding, Z. Zhang, Z. Zhao, et al., Multiband switchable microwave absorbing metamaterials based on reconfigurable kirigami–origami, Adv. Funct. Mater. **36**, e15206 (2025)
36. Y. Wang, X. Zhang, Y. Wang, et al., Recent advances in metasurfaces: from THz biosensing to microwave wireless communications, Research **8**, 0820 (2025)
37. J.M. Saca, Snell's law for light rays in moving isotropic dielectrics, Proc. IEEE **68**, 409 (1980)
38. M.V. Berry, The adiabatic phase and Pancharatnam's phase for polarized light, J. Mod. Opt. **34**, 1401 (1987)
39. X. Ma, Y. Duan, Y. Shi, et al., Broadband asymmetric transmission in quasiperiodic-metamaterials based on high entropy alloys ribbon, J. Alloys Compd. **946**, 169349 (2023)
40. L. Huang, Y. Duan, J. Liu, et al., Bioinspired gyrotropic metamaterials with multifarious wave adaptability and multifunctionality, Adv. Opt. Mater. **8**, 2000012 (2020)

41. Y. Shen, X. Wang, Z. Xie, et al., Optical vortices 30 years on: OAM manipulation from topological charge to multiple singularities, Light Sci. Appl. **8**, 90 (2019)
42. Z. Liao, J. Zhou, G. Luo, et al., Microwave-vortex-beam generation based on spoof-plasmon ring resonators, Phys. Rev. Appl. **13**, 054013 (2020)
43. M. Akram, G. Ding, K. Chen, et al., Ultrathin single layer metasurfaces with ultra-wideband operation for both transmission and reflection, Adv. Mater. **32**, 1907308 (2020)
44. C. Menzel, C. Rockstuhl, F. Lederer, Advanced Jones calculus for the classification of periodic metamaterials, Phys. Rev. A **82**, 053811 (2010)
45. L. Huang, Y. Duan, J. Liu, et al., Bionic composite metamaterials for harvesting of microwave and integration of multifunctionality, Compos. Sci. Technol. **204**, 108640 (2021)
46. Y. Duan, H. Pang, X. Wen, et al., Microwave absorption performance of FeCoNiAlCr0.9 alloy powders by adjusting the amount of process control agent, J. Mater. Sci. Technol. **77**, 209 (2021)
47. W. Song, X. Guan, L. Fan, et al., Strong and thermostable polymeric graphene/silica textile for lightweight practical microwave absorption composites, Carbon **100**, 109 (2016)
48. C. Xu, B. Wang, Y. Pang, et al., Hybrid metasurfaces for infrared-multiband radar stealth-compatible materials applications, IEEE Access **7**, 147586 (2019)
49. Y. Duan, B. Ma, L. Huang, et al., Moth-eye-inspired gradient impedance microwave absorption materials with multiband compatible stealth characteristic, Adv. Mater. Technol. **8**, 2202172 (2023)
50. Y. Duan, M. Wang, W. Chen, et al., Layered metamaterials with Sierpinski triangular fractal metasurface: compatible stealth for S-band radar and infrared, Mater. Today Phys. **38**, 101210 (2023)
51. J. Sui, J. Zhang, K. Yan, et al., Breaking bandwidth limit: all-medium metamaterial absorber engineered from heterostructure-anchored N-doped hollow carbon spheres, Chem. Eng. J. **524**, 169301 (2025)
52. T. Zhang, Y. Duan, J. Liu, et al., Tailoring the resonances on Fibonacci spiral fractal metasurface for miniaturized multiband microwave applications, Opt. Commun. **518**, 128353 (2022)
53. C. Xu, B. Wang, M. Yan, et al., An optically transparent sandwich structure for radar-infrared bi-stealth, Infrared Phys. Technol. **105**, 103108 (2020)
54. P. Liu, L. Wang, B. Cao, et al., Designing high-performance electromagnetic wave absorption materials based on polymeric graphene-based dielectric composites: from fabrication technology to periodic pattern design, J. Mater. Chem. C **5**, 6745 (2017)

Cite this article as: Zhufang Hao, Yupeng Shi, Yuping Duan, Integrating vortex wave generation with broadband microwave attenuation using a multi-layer cascaded metasurface, EPJ Appl. Metamat. **13**, 15 (2026), https://doi.org/10.1051/epjam/2026004